ORIGINAL RESEARCH ARTICLE

Deformation Mechanisms of (100) and (110) Single-Crystal BCC Gum Metal Studied by Nanoindentation and Micropillar Compression

DARIUSZ M. JARZĄBEK, MATEUSZ WŁOCZEWSKI, MICHAŁ MILCZAREK, PIOTR JENCZYK, NAOHISA TAKESUE, KAROL M. GOLASIŃSKI, and ELŻBIETA A. PIECZYSKA

In this paper, small-scale testing techniques—nanoindentation and micropillar compression—were used to investigate the deformation mechanisms, size effects, and strain rate sensitivity of (100) and (110) single-crystal Gum Metal at the micro/nanoscale. It was observed that the (100) orientation exhibits a significant size effect, resulting in hardness values ranging from 1 to 5 GPa. Conversely, for the (110) orientation, this effect was weaker. Furthermore, the yield strength obtained from the micropillar compression tests was approximately 740 MPa for the (100) orientation and 650 MPa for the (110) orientation. The observed deformations were consistent with the established features of the deformation behavior of body-centered cubic (bcc) alloys: significant strain rate sensitivity with no depth dependence, pile-up patterns comparable to those reported in the literature, and shear along the {112}<111> slip directions. However, the investigated material also exhibited Gum Metal-like high ductility, a relatively low modulus of elasticity, and high yield strength, which distinguishes it from classic bcc alloys.

https://doi.org/10.1007/s11661-024-07605-3

I. INTRODUCTION

ONE of the driving forces in engineering is enhancing the mechanical performance of materials. This pursuit is especially crucial for newly developed materials, as there is a critical need to comprehend their underlying phenomena. Investigating the fundamental aspects of deformation can significantly accelerate advancements in both industrial and everyday life applications. Materials exhibiting superelasticity and a low elastic modulus, yet with high strength, are especially sought after for various applications, such as prostheses in biomedicine or storage tanks in the fuel industry. These materials can withstand mechanical stress without experiencing failure. In prostheses, their importance lies in establishing a reliable connection between bones and bioimplants.[1] In the storage of hazardous liquids, their presence is crucial for maintaining the integrity of the tank and preventing leakage.[2]

A new class of materials, widely referred to as Gum Metal, was introduced in 2003 by Saito *et al.*[3] as a promising solution for meeting the above-mentioned requirements. Gum Metals are body-centered cubic (bcc) Ti-based with alloying elements, such as Nb, Ta, V, Zr, Hf, and O. According to Reference 3, the defining characteristics of Gum Metals are as follows: (1) a compositional average valence electron number [electron/atom (e/a) ratio] of about 4.24; (2) a bond order (B_o value) of about 2.87; and (3) an electronegativity M_d of about 2.45 eV. Additionally, Reference 4 imposes a fourth requirement: (4) an equivalent β stabilizer content $Mo_{eq} \approx 10$ (10.0 to 10.9) wt pct. Although the first study reported polycrystalline bcc structures, further studies found bcc lattices combined with nanosized hexagonal and orthorhombic phases.[4] These characteristics result in high elasticity, ductility, and yield strength of this alloy. However, its extraordinary properties are due not only to its composition but also its microstructure. If the alloy is tested after severe cold working, its shear strength seems to approach the ideal value.[5] Recent research on Gum Metal has revealed

DARIUSZ M. JARZĄBEK is with the Institute of Fundamental Technological Research, Polish Academy of Sciences, 02-106 Warsaw, Poland and also with the Warsaw University of Technology, 00-661 Warsaw, Poland. Contact e-mail: djarz@ippt.pan.pl MATEUSZ WŁOCZEWSKI is with the Warsaw University of Technology. MICHAŁ MILCZAREK, PIOTR JENCZYK, and ELŻBIETA A. PIECZYSKA are with the Institute of Fundamental Technological Research, Polish Academy of Sciences. NAOHISA TAKESUE is with the Fukuoka University, Fukuoka 814-0180, Japan. KAROL M. GOLASIŃSKI is with the Multidisciplinary Research Centre, Cardinal Stefan Wyszyński University in Warsaw, 05-092 Dziekanow Lesny, Poland.
Manuscript submitted April 24, 2024; accepted September 19, 2024.

Published online: 01 October 2024

complex behavior—ordinary dislocation flow, deformation twinning, and transformation-induced plasticity.[6,7] Hence, to understand Gum Metal's unusual behavior, it is vital to first investigate deformation in a simpler system, such as in a single crystal. It has been already revealed that, contrary to the previously proposed non-dislocation deformation at the ideal shear strength, single crystals of Gum Metal at the macroscale behave quite consistent with the established features of deformation behavior of other bcc alloys.[7] It was observed that it has strongly temperature-dependent yield stress below room temperature by the Peierls mechanism, weak temperature-dependent yield stress above the room temperature by the alloy hardening mechanism, and {112} slip asymmetry when it deforms.[8] Takesue *et al.*[8] observed significant nonlinearity and hysteresis during tensile tests along the <110> direction. Moreover, according to Morris *et al.*[9] and Takesue *et al.*,[8] both the mechanical response and the dominant deformation behavior change with the sign and orientation of the applied stress. Kimimura *et al.*[8] pointed out that the basic deformation mechanism via the Peierls mechanism in compression may be the same for mono- and polycrystals.[7] Contrary to this, a single crystal under tension was proved to exhibit Gum Metal properties due to reversible stress-induced transformations both of the bcc matrix and B2 nanoclusters.[3] This was observed in other Ti-based alloys.[10] It was shown that microstructural condition may influence these phase transformations.[11] Moreover, the deformation mechanism may be changed by introducing pre-deformation[12] or internal stresses.[13] Nonetheless, for those mechanisms, strain rate sensitivity (SRS) may be relatively high.[3,7] While SRS has been investigated comprehensively in HCP Ti-based alloys,[14–16] the changes in deformation mechanisms due to strain rate changes are not well-investigated bcc Ti-based gum metals. Those changes may depend on single-crystal orientation as sounding anisotropy was reported.[17] While $E_{100} < E_{110} < E_{111}$, non-linear elasticity and hysteresis were observed only in the <110> direction.[8] The phase transformation dependence of the size effect was studied;[18] however, strain rate and its influence on deformation mechanism in single crystal are yet to be understood.[19] In polycrystalline Gum Metal, deformation is influenced by the strain rate: a lower strain rates lead to uniform deformation, while higher strain rates cause relatively soon strain localization.[20] Hence, in tensile tests, strain hardening was observed at lower strain rates in contrast to strain softening at higher strain rates.[21]

Few researchers have addressed the problem of the behavior of the Gum Metal at the micro/nanoscale.[22–25] Of particular note is Withey's *et al.* work, which investigated nanoindentation and nanopillars compression of the cold-worked and next annealed Gum Metal.[23–25] They have observed unusual deformation patterns, *i.e.,* the cold-worked alloy deformation occurred with no evidence of dislocation, twin, or fault propagation into the bulk. Hence, understanding the influence of confined volumes and high surface ratios can be very useful for predicting and improving the Gum Metal performance. In particular, nanoindentation is uniquely suited for studying failure at the ideal strength in shear, which, to-date, has been observed in severely cold-worked Gum Metal and can occur even in the as-produced single crystals.[22] Therefore, in this study, small-scale testing techniques, *i.e.*, nanoindentation and micropillars compression, were used to investigate deformation mechanism and strain rate sensitivity of single-crystal Gum Metal at the micro/nanoscale.

II. EXPERIMENTAL

A. *Samples Preparation and Characterization*

Single-crystal ingots with two orientations (100) and (110) were grown from the master alloys Ti–36Nb–2-Ta–3Zr–0.3O (wt pct) using an optical floating zone apparatus (four mirror type, FZ-T-4000-H, Crystal Systems Inc.) at a crystal growth rate of 6.0 mm h^{-1} under a high-purity argon gas flow.[8] Next, the samples were cut using an electric discharge machine and precisely polished with the use of a vibropolisher so that their surfaces were free of the internal stresses usually introduced by classical polishing techniques. Finally, FESEM-FIB ZEISS Crossbeam 350 was used for sample characterization. It was equipped with an EDAX EDS detector, which allows for elemental composition determination, and an EDAX EBSD camera for microstructure investigation and the precise determination of the crystallographic orientations.

B. *Nanoindentation*

1. *Hardness measurement*

The nanoindentation of the samples was performed on the ALEMNIS Nanoindentation Tester placed in the chamber of the FESEM-FIB ZEISS Crossbeam 350. The measurements were performed in a high vacuum. Nanoindentation was performed by the nanoindentation tester equipped with a three-sided pyramidal diamond Berkovich's indenter. Indentations with five different loading rates were performed, namely 0.1, 1, 10, and 100 mN/min. The sampling rate was 200 Hz. The size effects were studied by application of maximum indentation loads in the range from 1 up to 30 mN. The value of hardness and Young's modulus was determined by the Oliver–Pharr method, a standard procedure for determining these properties from the nanoindentation load–displacement curves.[26]

The equipment in the test setup benefits from the SEM vacuum chamber and precise temperature control within the lab, resulting in minimal drift of the displacement and load. Nonetheless, additional data correction is necessary to ensure the highest quality of the hardness and indentation modulus determination. Alemnis Materials Mechanics Data Analyzer, software provided by the nanoindenter manufacturer, was used for data correction and analysis. The analyzer works as follows. First, displacement thermal drift value is measured using a special "hold" section during an experiment. The section is added during unloading at a

load level of 10 pct of the maximum load before complete unloading. The software then measures displacement thermal drift during the hold segment and subtracts it proportionally from the whole measured curve. The procedure is shown in Figure 1(a) where I is the measured load–displacement curve before correction with visible correction hold segment and II is the actual load–displacement curve after correction. It should be emphasized that the hardness is then determined using part of the unloading curve above the holding segment.

Next, the load drift correction was performed. To subtract the load drift from the results, a line was fitted to the points at the beginning and end of the load–time graph, assuming a linear time dependence of the load drift. Subsequently, this fitted line was subtracted from the measured displacement to obtain the actual displacement. The procedure is shown in Figure 1(b), where I is the fitted line, II is the actual displacement after correction, and III is the measured displacement before correction. Sections marked on graph are as follows: 1—approach; 2—loading; 3—unloading with tip still in contact with sample; and 4—retracting with tip no longer in contact with the sample. Finally, the overall procedure of indentation is presented in Figure 1(c). In the graph, section 1 is the approach. It comprises subsegment 1a when the tip is not in contact with the sample (displacement control) and subsegment 1b when the tip is in contact with the sample (load control). Section 2 is a short hold (1 second) with maximum load for ensuring lack of significant creep during unloading. Section 3, which is the unloading stage is divided into 3a—partial unloading, 3b—correction hold, and 3c—complete unloading.

Finally, it should be noted that the yielding due to the holding segment contributes to the displacement, the final shape of the imprints, the pile-up pattern, and the strain field under the imprints. Therefore, for the lowest strain rates (0.001 and 0.0001 s^{-1}), a minimum of three imprints without the holding segment were prepared for investigation with the atomic force microscope (AFM) and transmission Kikuchi diffraction (TKD).

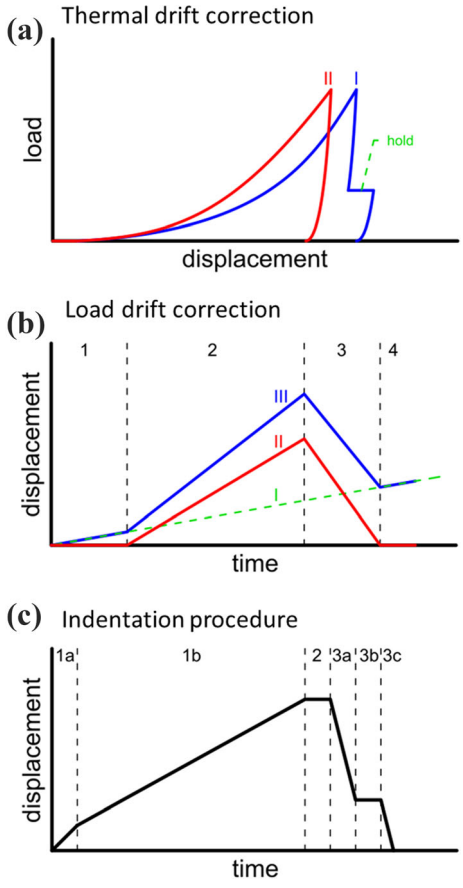

Fig. 1—Indentation experiments. (*a*) Thermal drift correction; (*b*) load drift correction; and (*c*) indentation procedure.

2. *Nanoindentation strain rate sensitivity*

Strain rate sensitivity (SRS) provides information about the influence of the strain rate on material properties, such as hardness. From the nanoindentation experiments, SRS_{ind} can be determined with the following equation:

$$SRS_{ind} = \frac{\partial \ln H}{\partial \ln \dot{\varepsilon}_{ind}}, \quad [1]$$

where H is the hardness and $\dot{\varepsilon}_{ind}$ is the indentation strain rate. According to Reference 1, $\dot{\varepsilon}_{ind}$ is defined as

$$\dot{\varepsilon}_{ind} = \frac{\dot{P}}{2P}, \quad [2]$$

where P is the maximum applied load and $\dot{P}$ is the load rate. In order to determine SRS_{ind}, we have plotted $\ln H$ *vs* $\ln \dot{\varepsilon}_{ind}$ and performed the linear fit. SRS_{ind} is then equal to the slope of the fitted straight line (Figure 2).

3. *Pile-up pattern investigation*

The imprints created during nanoindentation were later imaged with the use of an atomic force microscope (AFM) in order to thoroughly analyze details, such as pile-up and sink-in. The deformation of the material around the contact area, *i.e.*, sinking -in (deformation downward with respect to the indented surface plane) and piling up (deformation upward), are correlated with

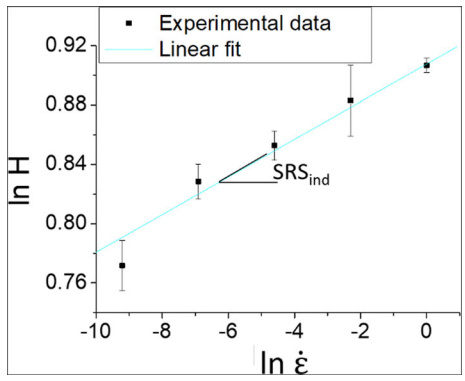

Fig. 2—An example of determination of SRS_{ind} obtained by indentation of (110) Gum Metal single crystal with 30-mN maximum load.

the material properties.[27] In this study, the imprints were scanned with the use of Nanosurf FlexAFM in the contact mode. The normal load was equal to a few tens of nanonewtons, and the scanning speed was 10 μm/s. The obtained data were analyzed using the Gwyddion open-source software.[28] Raw images were leveled by mean plane subtraction, and rows were aligned using the median method. Afterward, four profiles were extracted: one on the surface and three going through the center of the imprint and one of the vertices (Figure 3). The height of the pile-up patterns is the average height of the highest pile-up determined from difference in height between the surface (profile 4) and profiles 1 to 3.

C. *Simple and Cyclic Micropillars Compression*

The mechanical behavior of materials at the nanoscale exhibits sensitivity to not only microstructure and specimen size but also the geometry and constraint of the specimen and the volume undergoing deformation. Hence, for a broader view of the mechanical properties at the nanoscale nanoindentation is not sufficient, and additional tests such as the micropillar compression test should be performed. In this study, nine pillars, each with an 800 nm diameter, were prepared by focus ion beam (FIB) milling for both studied crystallographic orientations. The typical process flow of the process involved milling rings in the material, starting at the outer diameter and progressing toward the center. Milling was performed in three steps: coarse (30 kV, 3 nA), slow (30 kV, 200 pA), and precise (30 kV, 2 pA) milling. Next, three strain rates, 0.1, 0.01, and 0.001 s^{-1}, were applied. Hence, three micropillars were compressed for each set of parameters. Displacement control was applied. To determine the compression strength, plots of the engineering stress versus engineering strain were made. In this case, the offset yield point (stress at 0.2 pct deformation) was taken as the compression strength [Figure 4(a)]. The pillars were also imaged before [Figure 4(b)] and after the compression [Figure 4(c)] to ensure that the experiment ran correctly. The images "after" were also used to investigate the deformation mechanisms.

Additionally, three pillars, each with a diameter of 800 nm, were prepared for both orientations to perform cyclic compression tests. In this case, the displacement control was also applied; however, the displacement in each cycle was precisely set to ensure the same conditions for all the investigated pillars. First, the indenter tip was carefully positioned over the pillar and then the indenter gradually approached the sample in 5-nm steps until contact was detected. In the first cycle, a displacement of 50 nm was achieved. In subsequent cycles, the displacements achieved were as follows: 100, 150, 200, and 250 nm. The maximum displacement corresponds to about 15 pct of the compression strain. The strain rate in the cyclic compression was set to 0.01 s^{-1}.

III. RESULTS

To elucidate the mechanical behavior of Gum Metal at the nanoscale and its similarities and differences to those of standard bcc single crystals, we investigated the size effects and influence of the strain rate through nanoindentation and micro-pillar compression tests. Specifically, we studied the hardness and yield strength for two Gum Metal monocrystals with crystallographic orientations (100) and (110).

In Figure 5, the results of energy-dispersive X-ray spectroscopy (EDS) and electron backscatter diffraction (EBSD) performed on both samples are shown. From the EDS maps, it is clear that the specimens were fabricated without any precipitates or other imperfections. According to the pole figures, obtained with EBSD, the crystallographic orientations of the samples

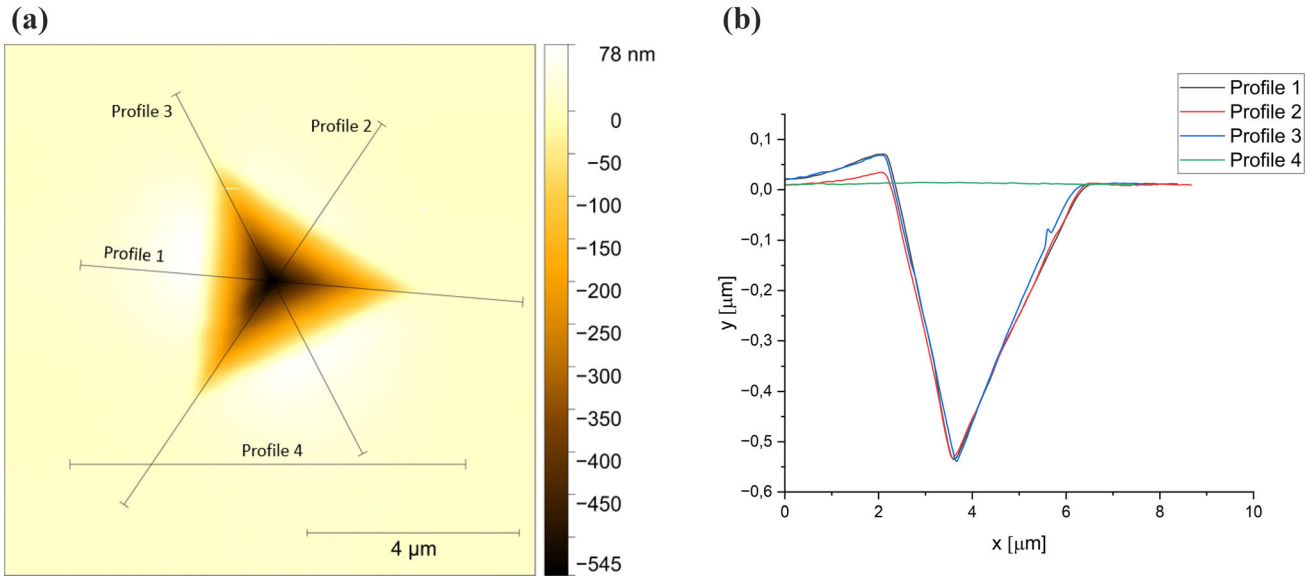

Fig. 3—Pile-up pattern investigation with the use of an AFM: (*a*) AFM image with the profiles indicated and (*b*) cross-sections through the imprint for determination of the pile-up height (each profile is averaged over 10 pixels in width of a line).

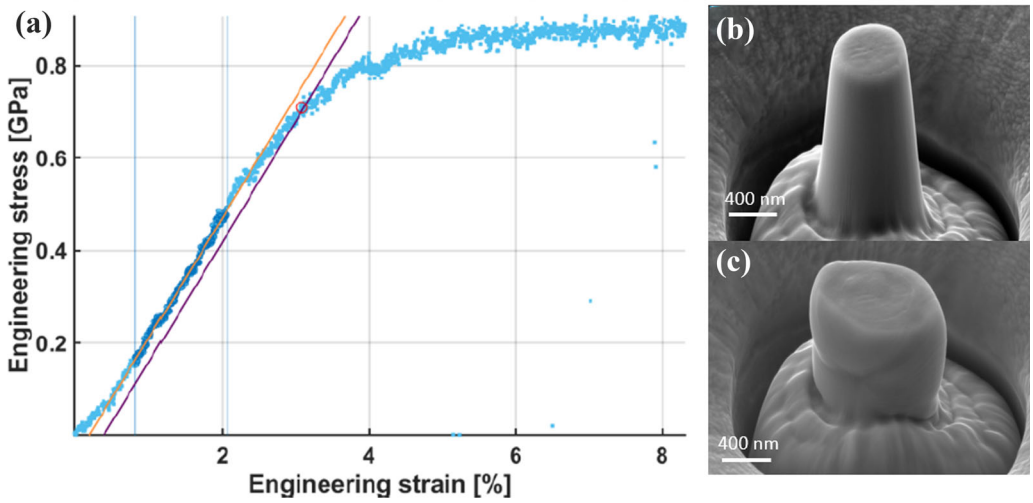

Fig. 4—Micropillar compression. (*a*) The plot and methodology of the yield point determination; (*b*) a pillar before; (*c*) and after compression.

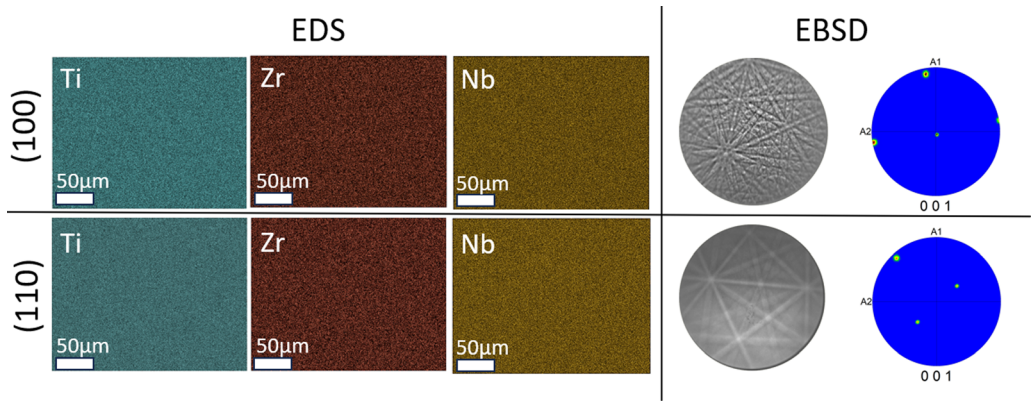

Fig. 5—Results of EDS and EBSD measurements.

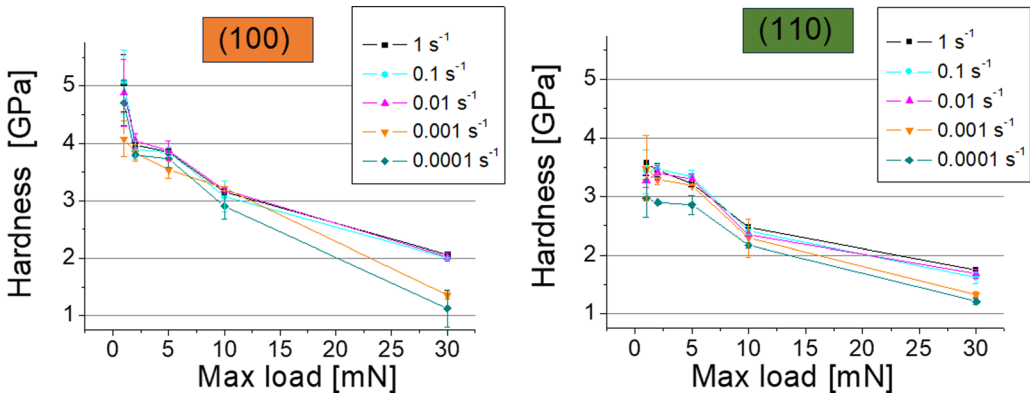

Fig. 6—Results of hardness measurement with different loads and strain rates both orientations. The lines connecting the points are a "guide for the eye".

were very close (orientation accuracy ≤ 0.7 deg) to the assumed and desired orientations (100) and (110).

The results of hardness measurements of both orientations are shown in Figure 6. The exact hardness values are provided in electronic supplementary Table 1 and 2SI. It is clearly visible that the hardness in the (100) orientation is higher than in the (110) direction, especially in the case of smaller loads. It is between 4 and 5 GPa for the (100) orientation and between 3 and 3.5 GPa for the (110) orientation depending on the strain

rate. For higher strain rates, the hardness is higher. However, for higher maximum loads, hence deeper indentation depths, this difference becomes less significant. It is then clear that the (100) orientation exhibits a much stronger size effect. It should be also noted that the creep observed during the holding of the maximum force was insignificant, even for the imprints with the highest strain rate it did not exceed 3 pct of the displacement during loading.

The results of the SRS_{ind} determination are shown in Figure 7(a). For the (110) orientation, SRS_{ind} is equal to approximately 0.02 for all the applied maximal loads, whereas for the (100) orientation, it is much lower. If we look closely at the measurement errors, we can claim that SRS_{ind} is close to 0 for the (100) orientation. SRS_{ind} also does not depend on the maximum applied load; hence, it does not depend on the depth. Additionally, the pile-up height reported in Figures 7(b) and (c), both for the lowest and the highest loads, is significant and equal to approximately 10 pct of the indentation depth. The AFM images of the imprints (Figure 8 at the top) and pile-up patterns (Figure 8 at the bottom) give us insight into the formation of the pile-up. It should be noted that pile-ups tend to exhibit similar heights for all three sides of the imprint for higher rates (1 s^{-1}). For lower strain rates, there is one pile-up that is significantly higher than the rest.

According to the Oliver–Pharr method, one can also determine the modulus of elasticity from the indentation curve. In this study, we did not observe any dependence on the applied load or strain rate. The modulus of elasticity was equal to 93 ± 12 GPa for the (100) orientation and was slightly lower (86 ± 11 GPa) for the (110) orientation.

In Figure 9, the results of pillar compression are shown. In Figure 9(a), representative results for pillars compressed with a 0.01 strain rate are presented for both orientations. The results obtained with different strain rates are similar, and the differences are in the range of the measurement error. In Figure 9(b), the average compression strength is provided. It is higher for the (100) orientation than for the (110) orientation, which is consistent with the hardness measurement. On the other hand, the (110) orientation exhibits strain hardening, whereas a decrease in stress is observed for the (100) direction. This decrease in stress is caused by intense shear of the pillar, which is visible in the SEM images. In Figure 9(c), the SEM images (on the left) and STEM cross-sections (on the right) of the compressed pillars are shown. The slip planes are clearly visible in the SEM images. In the STEM images, the slip traces corresponding to the theoretical slip directions of bcc crystals are indicated. For (100) orientation, the slip occurred only along $(21\bar{1})[\bar{1}1\bar{1}]$ direction. In almost all the performed compression tests, the fracture occurred, and a typical "hat" was created. In contrast, the (110) orientation deformed plastically via double slip. This was expected because the (110) orientation in bcc metals has two high Schmid factor slip planes and two inactive slip planes. The deformation mechanism was also confirmed by transmission Kikuchi diffraction (TKD) performed on the pillars cross-section. Crystallographic orientations are uniform, without any sign of twinning. Furthermore, both STEM and TKD have not provided any evidence on dislocation activity.

The results of cyclic compression of the micropillars are shown in Figure 10. The differences in pillar behavior are again clearly evident. First, in the case of the (100) orientation, the hysteresis during unloading–loading is much smaller than that for the (110) orientation. Second, when significant shear occurs in the pillar with the (100) orientation, which can be seen in both the stress–strain curve (sudden decrease in stress at a strain of approximately 13 pct) and in the image of the pillar after compression, slip along the $(21\bar{1})$ slip plane can be observed. However, this effect is not observed for the pillar with the (110) orientation. These pillars do not

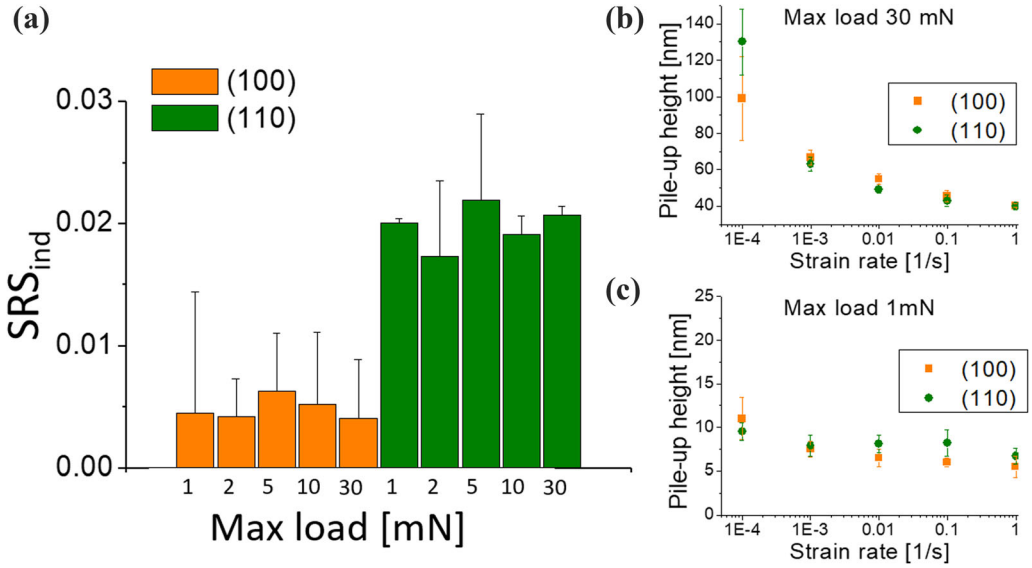

Fig. 7—SRS_{ind} and pile-up height. (*a*) SRS_{ind} *vs* maximal load; (*b*) height of the highest pile-up *vs* strain rate for a 30-mN maximal load; (*c*) height of the highest pile-up *vs* strain rate for a 1-mN maximal load.

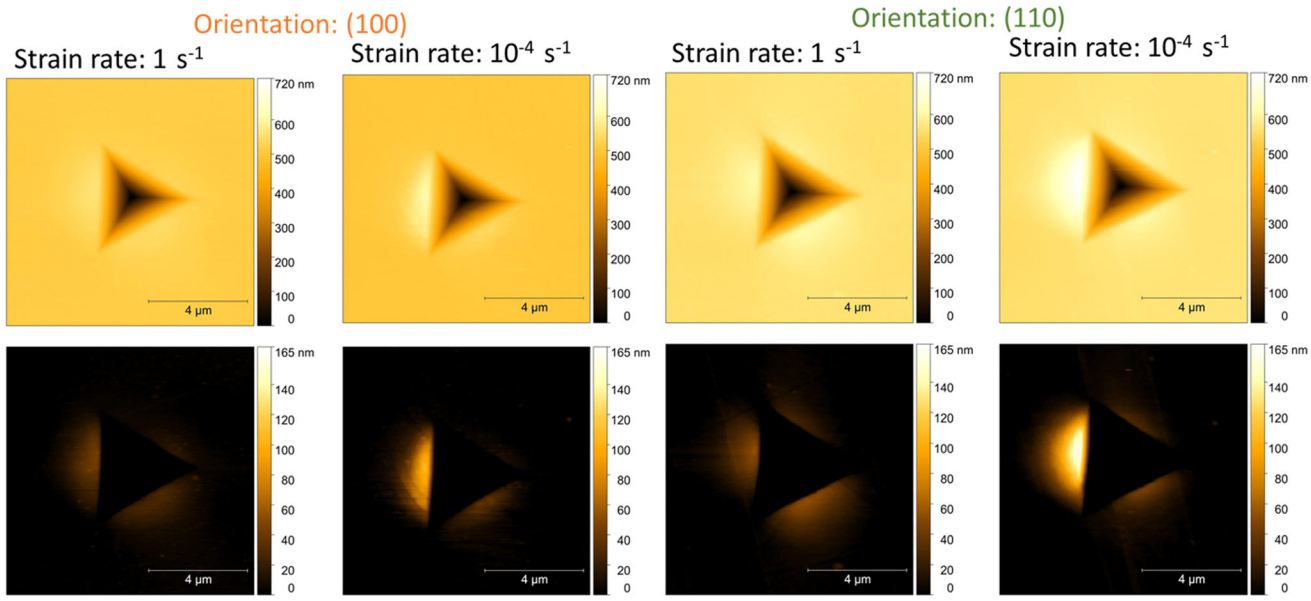

Fig. 8—AFM images of the nanoindentation imprints (at the top) and pile-up patterns (at the bottom).

fracture until a strain of approximately 16 pct and exhibit relatively higher strain hardening compared to those with the (100) orientation. In the SEM image, one can again see slips along the two {122}<111> slip systems; however, none of them lead to fracture. For a better understanding, we took photos of the pillars from two sides—the initial side and rotated by 90 deg. Two slip planes can be observed. From one side, the intersection of the planes is visible, while from the other side, the intersection between one slip plan and the pillar's outer surface can be observed. It should be indicated that similar results were observed for all the investigated pillars.

IV. DISCUSSION

Gum Metal is characterized by a low modulus of elasticity and high strength. For the single crystals investigated in this study, the modulus of elasticity was equal to 93 ± 12 and 86 ± 11 GPa for the (100) and (110) orientations, respectively. Similar values of Young's modulus for this material were obtained on polycrystalline samples by Sankaran *et al.*[22] (86 GPa) and Golasiński *et al.* (78 GPa).[29] Other papers in which similar alloys were investigated reported that the (100) orientation exhibits a significantly lower modulus of elasticity than the (110) orientation.[8,17] The reason for this difference may be differences in the methods used to calculate the elastic modulus. Typically, the elastic modulus is obtained from uniaxial tension/compression. However, in this study, we determined the modulus of elasticity from the nanoindentation unloading curve. In this case, the stress state is considerably more complex than that of the uniaxial tensile test, and it is widely recognized that this approach can yield higher values of the Young's modulus in comparison to classical tensile tests.[21]

The yield strength obtained from the micropillar compression tests is equal to approximately 740 MPa for the (100) orientation and 650 MPa for the (110) orientation, which is significantly higher than that of pure titanium and is comparable to data available in the literature for macroscopic experiments with the single-crystal Gum Metal. For example, Kamimura *et al.*[5] reported yield strength in compression tests equal to approximately 900 MPa for the (100) orientation and approximately 700 MPa for the (110) orientation.[7] Furthermore, one of the most important parameters of the Gum Metal, the yield strength-to-modulus ratio, which is shown in Figure 11(a), is between 7.5×10^{-3} and 8×10^{-3} (depending on the strain rate and crystallographic orientation) and is in line with the results obtained for other similar alloys. Kamimura *et al.*[5] reported yield strength-to-modulus ratio results of approximately 11.5 for the (110) orientation in macroscopic experiments. However, in the case of cold-swaged polycrystalline Gum Metal, the values were much higher, 19.5, owing to the much lower elastic modulus of the latter material.[7] Other similar polycrystalline materials were also investigated, and for Ti–33Nb–5.1Ta–7.1Z and Ti–29NB–13Ta–4.6Zr, the ratios were approximately 10 and 6, respectively.[30] The small differences between the results are most likely due to different specificities of the different measurement methods and scales. For example, as it was mentioned previously, nanoindentation provides a higher elastic modulus than macroscopic tensile tests. Another reason may be differences in oxygen concentration between different specimens, which is known to strongly affect the strength of Gum Metal.[4]

Furthermore, one can then determine the hardness-to-yield strength ratio. According to the empirical results present in the literature, it is equal to 2.8 for many metallic materials.[29,31] In Figure 11(b), the H/σ_y ratio is shown. Here, H is the hardness determined for a 30-mN

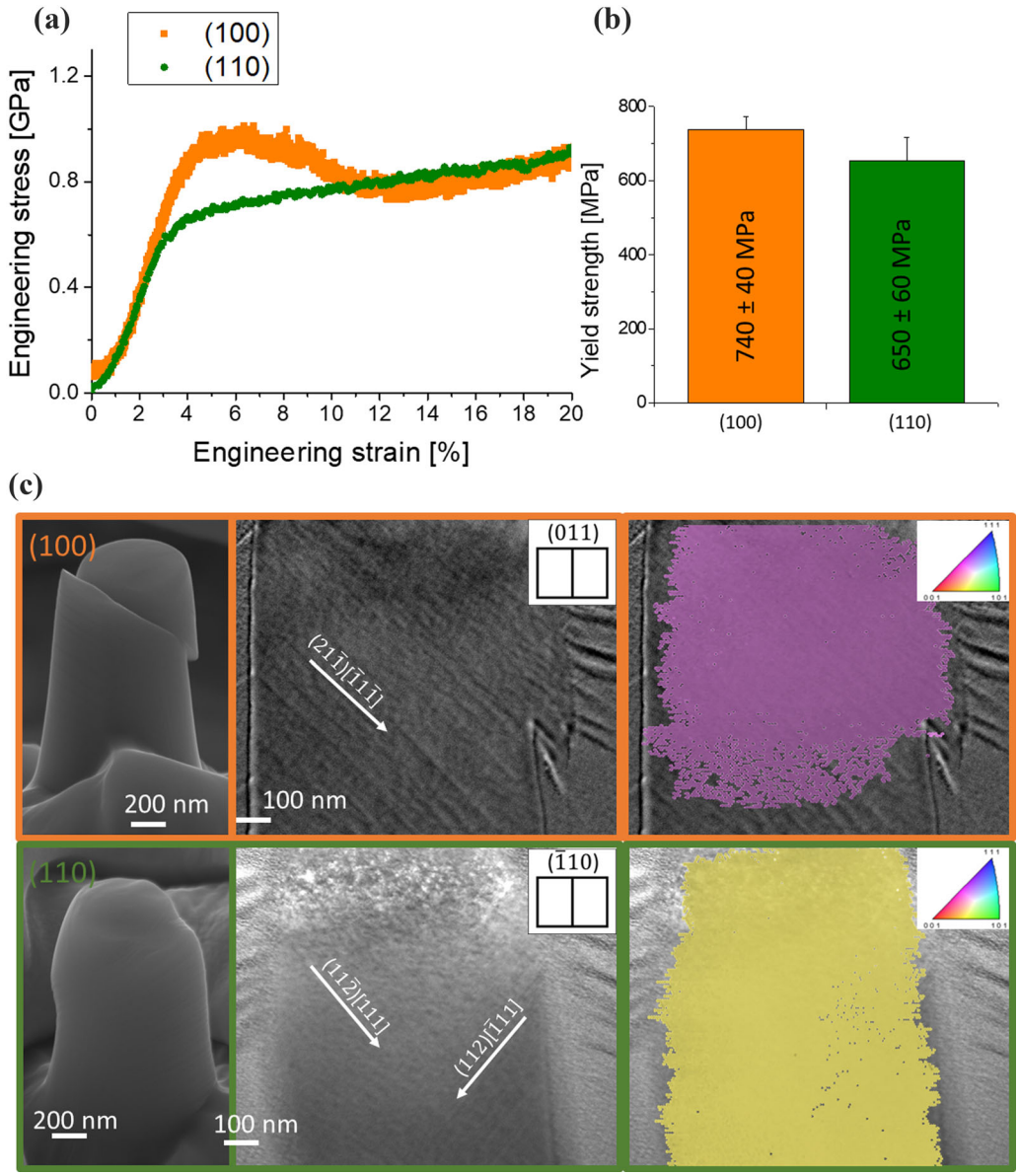

Fig. 9—Results of micropillar compression tests: (*a*) example of engineering stress *vs* engineering strain curves for both studied orientations; (*b*) results of the yield strength determination; (*c*) SEM (left), STEM images of the compressed pillars with indication of the slip directions (middle) and the same STEM image + crystallographic orientation of the pillars cross-section measured by TKD (right) (Color figure online).

maximal load, and σ_y is the compressive yield strength determined from micropillars compression. For all strain rates and for both orientations, this ratio is smaller than 2.8. The lowest values of H/σ_y are observed for the 0.001 s^{-1} strain rate for both studied orientations.[24]

For hardness, one can observe that the (100) orientation exhibits a significant size effect, which is considerably weaker for the (110) orientation. This result is consistent with the literature data on bcc single crystals[32] and is attributed to the higher amount of slip planes intersections and interlocking under the indenter for the (100) orientation.[33] The slip interlocking, which hardens the surface can be seen clearly in Figure 12, where the bright-field STEM images of the cross-sections of the imprints on the (100) orientation are shown. The deformation bands parallel to the traces of {112} planes intersect each other and interlock. Furthermore, the maps of the misorientation angle with respect to the initial orientation of the crystals [Euler angles (0,0,0)] are shown below the STEM images. The distributions of misorientation angles are slightly different for different strain rates, but the maximal values are similar. For lower strain rates, the misorientation spreads deeper under the imprint, which is in line with the lower hardness and higher pile-ups observed earlier.

According to Figure 7(a), there is no dependence of SRS_{ind} on the applied load/indentation depth. This result is again in line with the behavior of classical bcc alloys in which strain rate sensitivity is caused by a high lattice friction. This result demonstrates that, in this particular Gum Metal, in small dimensions, the thermally activated double kink mechanism is responsible

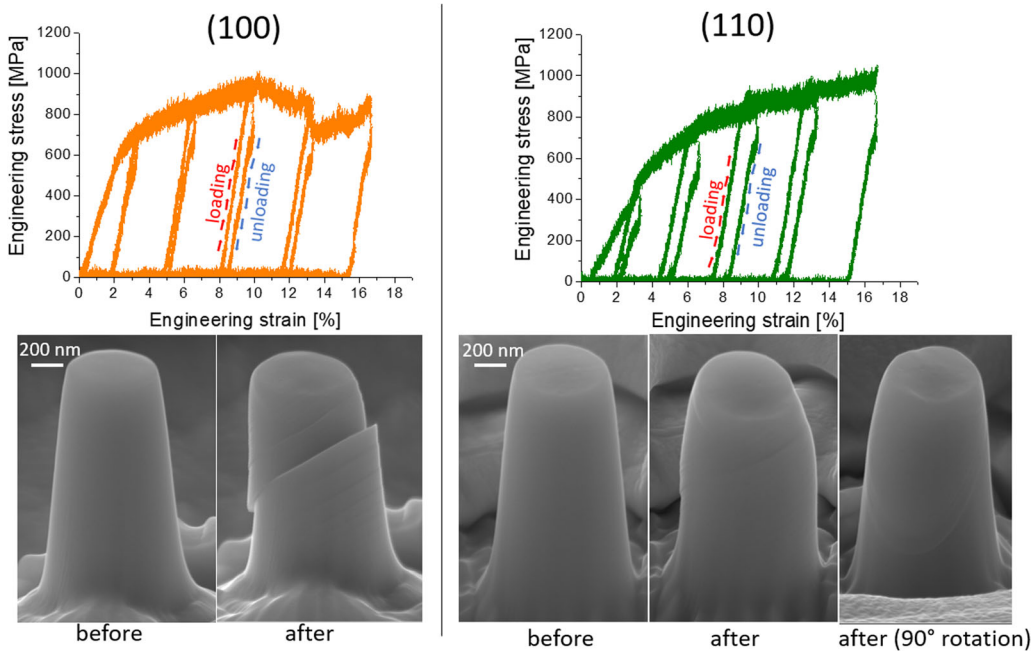

Fig. 10—Results of cyclic compression of the micropillars and corresponding SEM images of the pillars before and after compression. On the left—(100) pillar; on the right—(110) pillar.

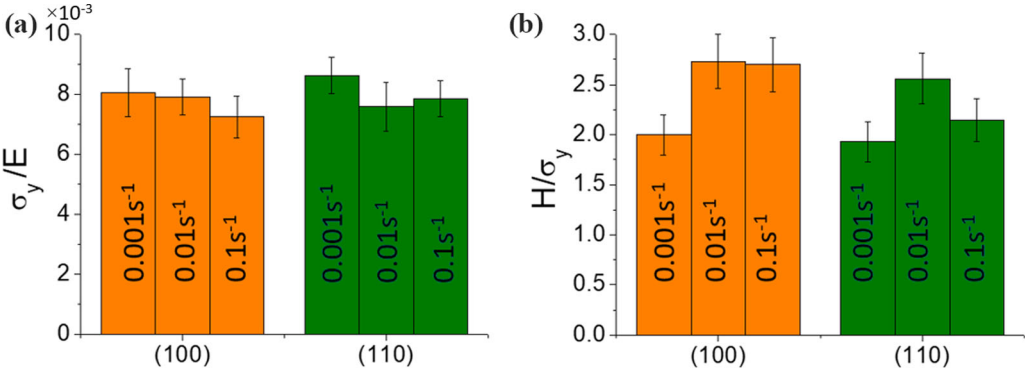

Fig. 11—Elastic-plastic properties of the investigated material for different strain rates: (*a*) yield strength-to-modulus ratio; and (*b*) hardness-to-yield strength ratio.

for the motion of screw dislocations and thus the deformation of the single crystal.[32]

In the case of bcc metals, slip is a complex phenomenon. Numerous experiments show that slip occurs in the closest packed <111> direction and that the Burgers vector is $a/2$<111>. The planes with the largest interplanar spacing are {110} followed by {112} then {123}.[34] According to Figure 9, where the results of micropillars compression are shown, and images from the top of the sample, in the studied Gum Metal, slip occurs in the <111> direction, and the slip planes are {112}, which is typical for bcc metals at the room temperature.[34] The reported yield strength of 740 MPa for the (100) orientation and 680 MPa for the (110) orientation are consistent with the hardness measurements that indicate that the (100) orientation is harder.

Furthermore, the single and cyclic compression tests revealed an intriguing difference in behavior of the pillars produced on different crystallographic orientations, which is not common for other bcc metals. For higher strains, the pillar at the (100) orientation exhibit sudden drop in the compression curve, which indicates a region of highly localized plasticity that causes plasticity induced shear failure, clearly visible in Figure 9 (orange). On the other hand, the pillar at the (110) orientation undergoes stable deformation without sudden failure and exhibit significant strain hardening. Furthermore, the latter pillar exhibits significant hysteresis during unloading–loading. Similar hysteresis was observed for single-crystal Gum Metal subjected to macroscopic tensile test by Takesue *et al.*,[8] and it was attributed to a martensitic transformation. However, it

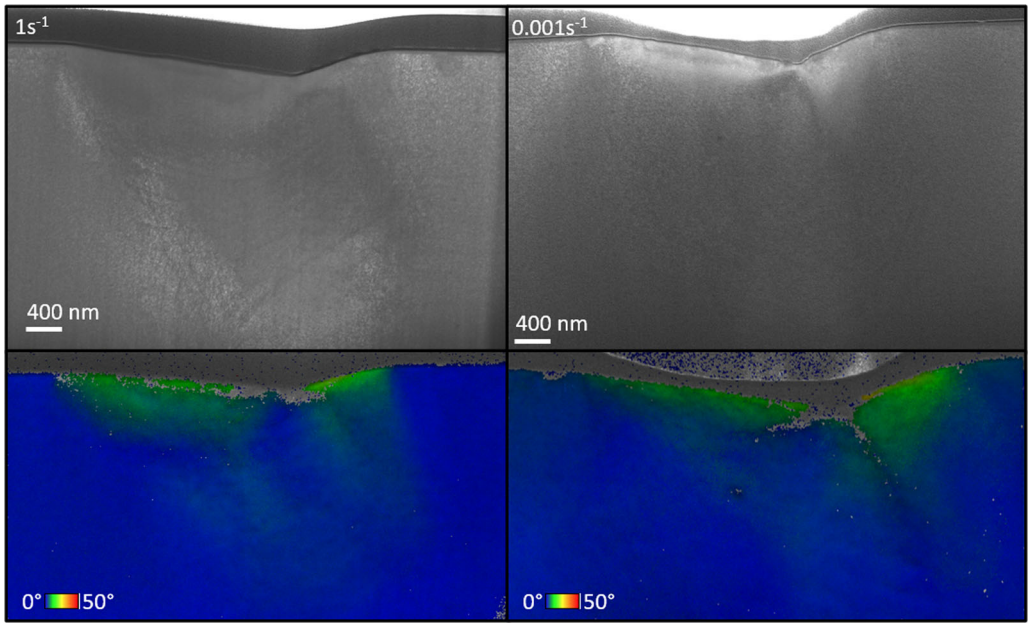

Fig. 12—Bright-field STEM images (top) and crystal misorientation determined from transmission Kikuchi patterns (bottom) for the cross-section of imprints performed on (100) orientation with two different strain rates.

should be noted that, in our case, the hysteresis loops close at the point of total unloading, *i.e.*, no elastic recovery is observed, which is significantly different from the results presented in Reference 8.

Finally, this paper presents observations of shear along the {112}<111> slip directions and it is in line with typical bcc single-crystal behavior. Similar results at the macroscale have been previously reported.[7] However, hysteresis loops during unloading–loading cycles and significant ductility in the case of (110) orientation points to more sophisticated deformation mechanism. This will be the subject of further research.

V. CONCLUSION

The strain rate sensitivity, size effects, and different mechanical behaviors at the micro/nanoscale of the (100) and (110) crystallographic orientation were studied for a Gum Metal single crystal. Both nanoindentation and micropillars compression were used, and the microstructure of the deformed samples was investigated. The observed deformations were consistent with the established features of the deformation behavior of bcc alloys: strong size effect, especially for (100) orientation; significant strain rate sensitivity with no depth dependence, pile-up pattern comparable to those reported in the literature, and shear along the {112}<111> slip directions. However, the investigated single crystals exhibited a high ductility, relatively low modulus of elasticity, and high yield strength, which is typical for Gum Metals. It should be noted that for the (110) orientation, the ductility was significantly higher, which was confirmed by pillar compression tests and an investigation of the pile-up patterns around the nanoindentation imprints.

SUPPLEMENTARY INFORMATION

The online version contains supplementary material available at https://doi.org/10.1007/s11661-024-07605-3.

ACKNOWLEDGMENTS

The authors would like to acknowledge the support of the National Science Center in Poland through Grants 2021/43/B/ST8/02895 and 2017/27/B/ST8/03074 for partially supporting the research. We would like to thank Editage (www.editage.com) for English language editing.

CONFLICT OF INTEREST

On behalf of all authors, the corresponding author states that there is no conflict of interest.

OPEN ACCESS

REFERENCES

1. M. Tanaka, M. Takemoto, S. Fujibayashi, T. Kawai, S. Yamaguchi, T. Kizuki, T. Matsushita, T. Kokubo, T. Nakamura, and S. Matsuda: *J. Mater. Sci. Mater. Med.*, 2014, vol. 25, pp. 635–43. https://doi.org/10.1007/s10856-013-5101-4.
2. S. Jamalpour Najmabad, M. Seyed Razzaghi, and F. Nateghi Alahi: *J. Press. Vessel. Pip.*, 2021, vol. 194, p. 104530. https://doi.org/10.1016/j.ijpvp.2021.104530.
3. T. Saito, T. Furuta, J.-H. Hwang, S. Kuramoto, K. Nishino, N. Suzuki, R. Chen, A. Yamada, K. Ito, Y. Seno, T. Nonaka, H. Ikehata, N. Nagasako, C. Iwamoto, Y. Ikuhara, and T. Sakuma: *Science*, 2003, vol. 300, pp. 464–67. https://doi.org/10.1126/science.1081957.
4. S. Yuan, N. Lin, Q. Zeng, H. Zhang, and Y. Wu: *Crit. Rev. Solid State Mater. Sci.*, 2023, vol. 48, pp. 257–88. https://doi.org/10.1080/10408436.2022.2050887.
5. T. Li, J.W. Morris, N. Nagasako, S. Kuramoto, and D.C. Chrzan: *Phys. Rev. Lett.*, 2007, vol. 98, p. 105503. https://doi.org/10.1103/PhysRevLett.98.105503.
6. V.A. Vorontsov, N.G. Jones, K.M. Rahman, and D. Dye: *Acta Mater.*, 2015, vol. 88, pp. 323–33. https://doi.org/10.1016/j.actamat.2015.01.033.
7. Y. Kamimura, S. Katakura, K. Edagawa, S. Takeuchi, S. Kuramoto, and T. Furuta: *Mater. Trans.*, 2016, vol. 57, pp. 1526–34. https://doi.org/10.2320/matertrans.M2016191.
8. N. Takesue, Y. Shimizu, T. Yano, M. Hara, and S. Kuramoto: *J. Cryst. Growth*, 2009, vol. 311, pp. 3319–24. https://doi.org/10.1016/j.jcrysgro.2009.03.052.
9. J.W. Morris, Y. Hanlumyuang, M. Sherburne, E. Withey, D.C. Chrzan, S. Kuramoto, Y. Hayashi, and M. Hara: *Acta Mater.*, 2010, vol. 58, pp. 3271–80. https://doi.org/10.1016/j.actamat.2010.02.001.
10. F. Niessen and E. Pereloma: *Adv. Eng. Mater.*, 2022, https://doi.org/10.1002/adem.202200281.
11. E.M. Hildyard, L.D. Connor, L.R. Owen, D. Rugg, N. Martin, H.J. Stone, and N.G. Jones: *Acta Mater.*, 2020, vol. 199, pp. 129–40. https://doi.org/10.1016/j.actamat.2020.08.004.
12. W. Zhang, P. Yang, X. Liang, Y. Cao, S. Ouyang, Y. Liu, and Z. Wu: *J. Alloys Compd.*, 2020, vol. 835, p. 155332. https://doi.org/10.1016/j.jallcom.2020.155332.
13. E.M. Hildyard, L.D. Connor, N.L. Church, T.E. Whitfield, N. Martin, D. Rugg, H.J. Stone, and N.G. Jones: *Acta Mater.*, 2022, vol. 237, p. 118161. https://doi.org/10.1016/j.actamat.2022.118161.
14. T.-S. Jun, D.E.J. Armstrong, and T.B. Britton: *J. Alloys Compd.*, 2016, vol. 672, pp. 282–91. https://doi.org/10.1016/j.jallcom.2016.02.146.
15. Z. Zhang, T.-S. Jun, T.B. Britton, and F.P.E. Dunne: *Acta Mater.*, 2016, vol. 118, pp. 317–30. https://doi.org/10.1016/j.actamat.2016.07.044.
16. T.-S. Jun, Z. Zhang, G. Sernicola, F.P.E. Dunne, and T.B. Britton: *Acta Mater.*, 2016, vol. 107, pp. 298–309. https://doi.org/10.1016/j.actamat.2016.01.057.
17. M. Tane, S. Akita, T. Nakano, K. Hagihara, Y. Umakoshi, M. Niinomi, and H. Nakajima: *Acta Mater.*, 2008, vol. 56(12), pp. 2856–63. https://doi.org/10.1016/j.actamat.2008.02.017.
18. Y. Pan, Q. Sun, L. Xiao, X. Ding, and J. Sun: *Mater. Sci. Eng. A*, 2019, vol. 743, pp. 798–803. https://doi.org/10.1016/j.msea.2018.11.140.
19. T. Furuta, S. Kuramoto, J.W. Morris, N. Nagasako, E. Withey, and D.C. Chrzan: *Scripta Mater.*, 2013, vol. 68, pp. 767–72. https://doi.org/10.1016/j.scriptamat.2013.01.027.
20. K. Golasiński, E. Pieczyska, M. Maj, M. Staszczak, P. Świec, T. Furuta, and S. Kuramoto: *Arch. Civ. Mech. Eng.*, 2020, vol. 20, p. 53. https://doi.org/10.1007/s43452-020-00055-9.
21. E. Pieczyska, M. Maj, K. Golasiński, M. Staszczak, T. Furuta, and S. Kuramoto: *Materials*, 2018, vol. 11, p. 567. https://doi.org/10.3390/ma11040567.
22. R.P. Sankaran, V.B. Ozdol, C. Ophus, J. Kacher, C. Gammer, S. Govindjee, A.M. Minor, and J.W. Morris: *Acta Mater.*, 2018, vol. 151, pp. 334–46. https://doi.org/10.1016/j.actamat.2018.03.048.
23. E.A. Withey, A.M. Minor, D.C. Chrzan, J.W. Morris, and S. Kuramoto: *Acta Mater.*, 2010, vol. 58, pp. 2652–65. https://doi.org/10.1016/j.actamat.2009.12.052.
24. E.A. Withey, M. Jin, A. Minor, S. Kuramoto, D.C. Chrzan, and J.W. Morris: *Mater. Sci. Eng. A*, 2008, vol. 493, pp. 26–32. https://doi.org/10.1016/j.msea.2007.07.097.
25. E.A. Withey, J. Ye, A.M. Minor, S. Kuramoto, D.C. Chrzan, and J.W. Morris: *Exp. Mech.*, 2010, vol. 50, pp. 37–45. https://doi.org/10.1007/s11340-008-9210-9.
26. W.C. Oliver and G.M. Pharr: *J. Mater. Res.*, 2004, vol. 19, pp. 3–20. https://doi.org/10.1557/jmr.2004.19.1.3.
27. M.A.G. Maneiro and J. Rodríguez: *Scripta Mater.*, 2005, vol. 52, pp. 593–98. https://doi.org/10.1016/j.scriptamat.2004.11.029.
28. D. Nečas and P. Klapetek: *Open Phys.*, 2012, vol. 10, pp. 181–88. https://doi.org/10.2478/s11534-011-0096-2.
29. K.M. Golasiński, R. Detsch, M. Szklarska, B. Łosiewicz, M. Zubko, S. Mackiewicz, E.A. Pieczyska, and A.R. Boccaccini: *J. Mech. Behav. Biomed. Mater.*, 2021, vol. 115, p. 104289. https://doi.org/10.1016/j.jmbbm.2020.104289.
30. Y. Fu, W. Xiao, J. Wang, L. Ren, X. Zhao, and C. Ma: *J. Mater. Sci. Technol.*, 2021, vol. 76, pp. 122–28. https://doi.org/10.1016/j.jmst.2020.11.018.
31. D. Tabor: *The Hardness of Metals*, The Clarendon Press, 1951, p. 1–18.
32. D. González, J. Alkorta, J.M. Martínez-Esnaola, and J. Gil Sevillano: *Comput. Mater. Sci.*, 2014, vol. 82, pp. 314–19. https://doi.org/10.1016/j.commatsci.2013.10.004.
33. J. Varillas, J. Očenášek, J. Torner, and J. Alcalá: *Acta Mater.*, 2021, vol. 217, p. 117122. https://doi.org/10.1016/j.actamat.2021.117122.
34. C.R. Weinberger, B.L. Boyce, and C.C. Battaile: *Int. Mater. Rev.*, 2013, vol. 58, pp. 296–314. https://doi.org/10.1179/1743280412Y.0000000015.